ACS APPLIED MATERIALS & INTERFACES

RESEARCH ARTICLE

www.acsami.org

# High-Yield Synthesis of Ultrathin and Uniform $Bi_2WO_6$ Square Nanoplates Benefitting from Photocatalytic Reduction of $CO_2$ into Renewable Hydrocarbon Fuel under Visible Light

Yong Zhou,*,† Zhongping Tian,† Zongyan Zhao,† Qi Liu,‡ Jiahui Kou,† Xiaoyu Chen,‡ Jun Gao,† Shicheng Yan,† and Zhigang Zou*,†

†Ecomaterials and Renewable Energy Research Center (ERERC), National Laboratory of Solid State Microstructures, School of Physics, and ‡Department of Materials Science and Engineering, Nanjing University, 22 Hankou Road, Nanjing, Jiangsu 210093, People's Republic of China

**ABSTRACT:** Ultrathin and uniform $Bi_2WO_6$ square nanoplates of ~9.5 nm thickness corresponding to six repeating cell units were prepared in the presence of oleylamine using a hydrothermal route. The $Bi_2WO_6$ nanoplates show great potential in the utilization of visible light energy to the highly efficient reduction of $CO_2$ into a renewable hydrocarbon fuel. On the one hand, the ultrathin geometry of the nanoplates promotes charge carriers to move rapidly from the interior to the surface to participate in the photoreduction reaction. This should also favor the improved separation of photogenerated electron and hole and a lower electron–hole recombination rate; on the other hand, the $Bi_2WO_6$ square nanoplate is proven to provide the well-defined {001} facet for two dominantly exposed surfaces, which is a prerequisite for the high level of photocatalytic activity of $CO_2$ fixation.

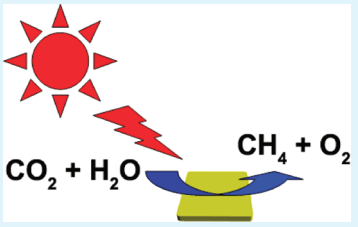


**KEYWORDS:** $Bi_2WO_6$, nanoplates, photocatalysis, visible light, $CO_2$ fixation, renewable fuel

## INTRODUCTION

$Bi_2WO_6$ as one of the simplest members of the Aurivillius family is composed of accumulated layers of corner-sharing $WO_6$ octahedral sheets and bismuth oxide sheets. $Bi_2WO_6$ as a visible-light-induced photocatalyst splitting water for $O_2$ evolution[1] and decomposing the organic contamination[2] revealed that $Bi_2WO_6$ could perform as excellent photocatalytic and solar-energy-transfer materials. Great progress has been made with the synthesis of various architectures of $Bi_2WO_6$, such as flowerlike microstructures.[3] The formation of deagglomerated, uniform, and monodisperse $Bi_2WO_6$ nanoplates, however, has been met with limited success, which is important to overcoming some difficulties in obtaining a high photocatalytic efficiency.

Increases of carbon dioxide ($CO_2$) in the atmosphere have become a global environmental issue because of their serious problems, such as the "greenhouse effect". The idea of mimicking the overall natural photosynthetic cycle of the chemical conversion of $CO_2$ into useful fuels has been consistently gaining attention for more than 30 years.[4−7] Such artificial photosynthesis allows the direct conversion of $CO_2$ and water on photocatalysts into valuable hydrocarbon using sunlight at room temperature and ambient pressure in order to to reduce atmospheric $CO_2$ concentrations while providing renewable carbon fixation and energy storage. Among the present photocatalysts for conversion, $TiO_2$-based semiconductor photocatalysts have been the most popular. Our $Zn_2GeO_4$ nanoribbons were recently demonstrated to exhibit promising photocatalytic activity for the reduction of $CO_2$ to $CH_4$.[8] However, both of them are only activated by ultraviolet light ($\lambda$ < 400 nm), which makes up about 4% of the solar spectrum. Several methods switch the photocatalytic activities of $TiO_2$ to the visible region, involving surface modification of the semiconductors by dopants,[9] organic dyes,[10] and transition-metal complexes.[11] Visible-light-absorbing metal sulfide semiconductors are unsuitable for photocatalytic reactions because they readily undergo photoanodic corrosion after extended light exposure. Thus, the development of sufficiently stable and efficient photocatalysts that can work under visible light is a strongly appealing challenge. Inspired by our pioneering production of $NiO_x/In_{0.9}Ni_{0.1}TaO_4$, splitting water into stoichiometric amounts of oxygen and hydrogen under visible-light irradiation,[12] we have successfully prepared a series of visible-light-responding oxide semiconductor photocatalysts.[13]

Here we report the high-yield production of ultrathin and uniform $Bi_2WO_6$ square nanoplates of ~9.5 nm thickness corresponding to six repeating cell units. We offer the potential of such ternary oxide nanoplates in the utilization of visible-light energy to a highly efficient reduction of $CO_2$ into a renewable hydrocarbon fuel. On the one hand, the ultrathin geometry of the nanoplates allows charge carriers to move rapidly from the interior to the surface to participate in the photoreduction reaction. This should also favor an improved separation of

Received: June 24, 2011
Accepted: August 4, 2011
Published: August 04, 2011

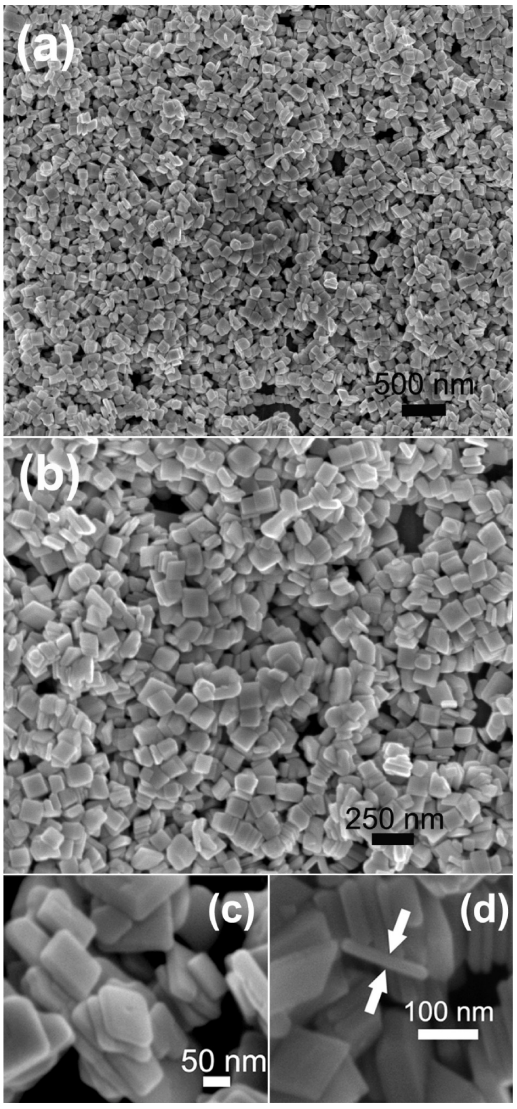


**Figure 1.** FESEM image of the $Bi_2WO_6$ square nanoplates at different magnifications. The arrows in part d show a standing square nanoplate.

photogenerated electron and hole and a lower electron−hole recombination rate; on the other hand, the $Bi_2WO_6$ square nanoplate proves to provide the well-defined {001} facet for two dominantly exposed surfaces, which is a prerequisite for the high level of photocatalytic activity of $CO_2$ fixation.

## EXPERIMENTAL SECTION

**Preparation of $Bi_2WO_6$ Nanoplates.** In a typical procedure, 1 mmol of $Bi(NO_3)_3 \cdot 5H_2O$ was added to 1 M $HNO_3$ to form a clear solution under stirring for 30 min at room temperature. Afterward, 25 mL of solution of dissolved 0.5 mmol of $Na_2WO_4 \cdot 2H_2O$, and 1 mL of $C_{18}H_{37}N$ was added into the above solution. The pH value of the suspension was adjusted to around 7 by adding $NH_3 \cdot H_2O$. The mixture was finally transferred into a 50 mL Teflon-lined autoclave and maintained at 200 °C for 20 h. The reactor was cooled to room temperature naturally. The resulting samples were collected and washed several times with acetone and deionized water and dried at 80 °C in air. The solid-state reaction (SSR) of $Bi_2WO_6$ was synthesized according to ref 2.

**Characterization.** The crystallographic phase of these as-prepared products was determined by powder X-ray diffraction (XRD; Rigaku Ultima III, Cu Kα radiation). The specific surface areas of the samples were measured by nitrogen sorption at 77 K on a surface area and porosity analyzer (Micromeritics TriStar) and calculated by the Brunauer−Emmett−Teller (BET) method. The morphologies of the samples were observed by a scanning electron microscope (FEI Tecnai G2 F30 S-Twin) and a transmission electron microscope (JEOL 3010, Japan). X-ray photoelectron spectroscopy (XPS) measurement was carried out with an ESCA Lab 250 spectrometer (Al Kα, 1486.6 eV). The XPS spectrum was calibrated with respect to the binding energy of the adventitious C 1s peak at 284.8 eV and was deconvoluted using *XPSPEAK* software. The BET surface area was measured on a Micromeritics TriStar surface area analyzer. The UV−vis diffuse-reflectance spectrum was recorded with a UV−vis spectrophotometer (Shimadzu UV-2550) at room temperature and transformed to the absorption spectrum according to the Kubelka−Munk relationship.

**Photocatalytic Conversion of $CO_2$ into $CH_4$.** In the photocatalytic reduction of $CO_2$, 0.1 g of the $Bi_2WO_6$ catalyst was uniformly dispersed onto the glass reactor with an area of 4.2 $cm^2$. A 300 W xenon arc lamp was used as the light source of the photocatalytic reaction. Light was passed through a UV cutoff filter ($\lambda > 420$ nm). The volume of the reaction system was about 230 mL. The reaction setup was vacuum-treated several times, and then the high purity of $CO_2$ gas was followed into the reaction setup for reaching ambient pressure. A total of 1 mL of deionized water was injected into the reaction system as the reducer. To ensure direct contact of the $Bi_2WO_6$ catalyst with $CO_2$ and gaseous water, the as-prepared photocatalysts were first treated in 500 °C to desorb the gas and burn off the surfactant residual on the surface and then allowed to equilibrate in the $CO_2/H_2O$ atmosphere for several hours to ensure that the adsorption of gas molecules was complete. During irradiation, about 0.5 mL of gas was continually taken from the reaction cell at given time intervals for subsequent $CH_4$ concentration analysis by using a gas chromatograph (GC-14B and GC8A; Shimadzu Corp., Japan). The quantification of the $CH_4$ yield was based on the external standard and the use of a calibration curve. Density functional theory (DFT) calculations were carried out by the Cambridge Serial Total Energy Package (CASTEP) codes. The ultrasoft pseudopotential was chosen to deal with the interaction between the ion core and valence electrons. The exchange and correlation effects among valence electrons were described by the Perdew−Burke−Ernzerhof basis set of the generalized gradient approximation. The Kohn−Sham wave functions of the valence electrons were expanded using a plane-wave basis set within a specified energy cutoff that was chosen at 340 eV. Also, the minimization algorithm was chosen as the Broyden−Fletcher−Goldfarb−Shanno scheme. In order to find the reaction path of $CO_2$ decomposition on the $Bi_2WO_3$ surface, we take the obtained molecular adsorption configuration as the reactant and the dissociative adsorption configuration as the product. To determine the activation energy for a specific reaction path, a transition state (TS) that connects two immediate stable structures through a minimum energy path was identified by complete synchronous transit (LST) and quadratic synchronous transit (QST) search methods followed by transition-state confirmation through the nudged elastic band method.

## RESULTS AND DISCUSSION

Field-emission scanning electron microscopy (FESEM) images show that the product is predominantly (>95%) the uniform $Bi_2WO_6$ square nanoplates with narrow size distribution (Figure 1a,b).

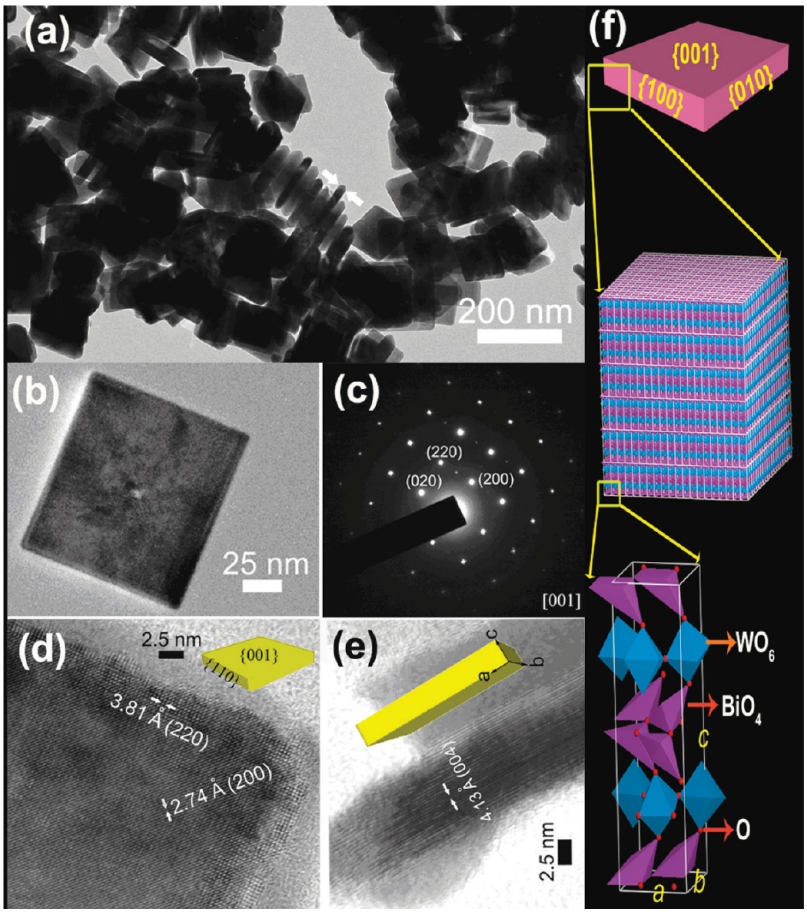


**Figure 2.** (a and b) TEM images of the $Bi_2WO_6$ square nanoplates, (c) SAED pattern, (d and e) HRTEM images for flat-lying and vertically standing nanoplates, respectively. (f) Corresponding structural model of the $Bi_2WO_6$ nanoplates.

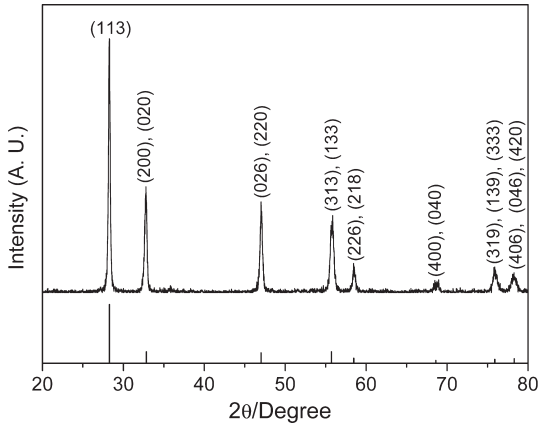


**Figure 3.** XRD pattern of the $Bi_2WO_6$ square nanoplates.

No other product morphologies were observed in the scanning electron microscopy (SEM) images, demonstrating the high-yield growth of the nanoplates. The high-magnification FESEM image reveals clear square contours of the nanoplates with a side length of ~120 nm (Figure 1c) and a thickness of ~9.5 nm (Figure 1d). The transmission electron microscopy (TEM) image further reveals that these nanoplates are regular square and nanoplate geometric shapes (Figure 2). The thickness is also measured about ~9.5 nm from the vertically standing nanplates, as shown by the arrows in Figure 2a. The selected area electron diffraction (SAED) pattern along the [001] zone of a typical nanoplate demonstrates the clear diffraction spots with well alignment, indicative of the single-crystal structure of the sheets (Figure 2b,c). The high-resolution TEM (HRTEM) image reveals that the square laminar shape grows preferentially along the {001} basal plane with a lattice fringe of $d_{(004)}$ = 4.13 Å and the {110} ($d_{(220)}$ = 3.81 Å) surrounding planes (Figure 2d,e). A crystalline model of the nanosquare can thus be schematically illuminated in Figure 2f. The thickness of the nanoplate is well corresponding to six repeating cell units, i.e., 6 × 1.65 nm = 9.90 nm.

XRD peaks of the $Bi_2WO_6$ nanoplate can be indexed to the orthorhombic $Bi_2WO_6$, which match very well with the reported data (JCPDS no. 73-1126; Figure 3). No impurity peaks are detected. The intensity ratio of the (200) or (020) peak to the (113) peak is 0.41, obviously larger than the standard value of 0.185, indicating that the crystal has special anisotropic growth along the (001) plane, in good agreement with the TEM observation. XPS analysis confirms that the Bi 4f peaks of the sample appeared at ca. 163.9 and ca. 158.7 eV and the W 4f peaks at 37.0 and 34.9 eV (Figure 4). The oxygen element has two kinds of chemical states: the crystal lattice oxygen at ca. 529.6 eV and the adsorbed oxygen at ca. 532.1 eV.[14]

To obtain a better understanding of the evolution process of the regular $Bi_2WO_6$ nanosquare, we trapped intermediate states

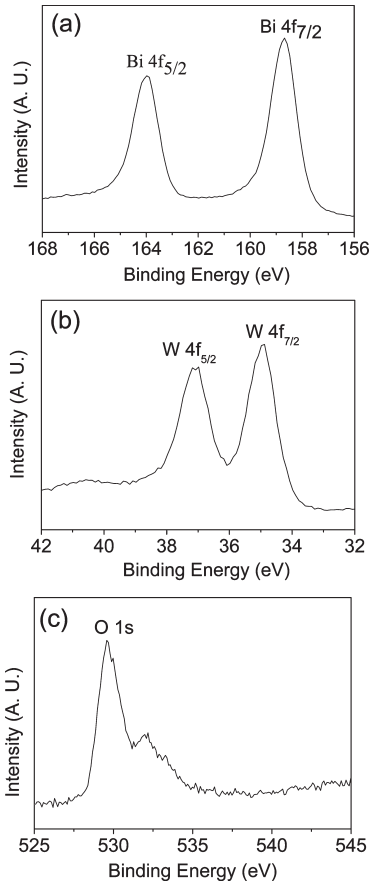


**Figure 4.** XPS spectra of the $Bi_2WO_6$ square nanoplates.

of the product. The tiny particles with diameter of 10−15 nm appear at the initial stage under hydrothermal conditions (Figure 5a). With prolonged time, these nanocrystals begin to grow into two-dimensionally thin platelike structures and stack together (as marked by the arrow in Figure 5b) because of the high intrinsic anisotropic properties of $Bi_2WO_6$. The primary $Bi_2WO_6$ particles continuously adsorb onto these growing plates with the Ostwald ripening process (Figure 5c) and then gradually ripen into single-crystal nanoplates (Figure 5d). The pH value of the solution has an important role in mediating the monondispersion of the nanoplate. The regular $Bi_2WO_6$ square flake can be produced between a pH of 6 and 9. A decrease of the pH to around 5.5 leads to serious in-plane and out-of-plane amalgamation of the nanoplate, and a large, irregular flake was formed at pH = 10.5 (Figure 6). We also found that, in the absence of oleylamine or by using surfactants such as cetyltrimethylammonium bromide (CTAB) and L-lysine rather than oleylamine, irregular flakes and their flowerlike aggregation were produced, which originate from the reduction of the interfacial energy surface (Figure 7). We believe that oleylamine may adsorb onto surfaces of the nucleating $Bi_2WO_6$ to regulate the lamellar growth and suppress the aggregation tendency of the growing plates.

The UV−vis diffuse-reflectance spectrum reveals that the absorption edge of the synthesized $Bi_2WO_6$ nanosquare extended to the visible-light region, which implies the possibility of high photocatalytic activity of these materials under visible-light illumination (Figure 8). The steep shape of the spectrum indicates that the visible-light absorption was not due to the transition from the impurity level but to the band-gap transition.[15] The absorption onset of the square nanoplate is at ca. 445 nm, corresponding to a band-gap energy of about 2.75 eV, mostly close to that of the SSR of $Bi_2WO_6$ (2.69 eV).[12] The position of the conduction band and valence band of the $Bi_2WO_6$ nanoplate could be calculated empirically according to eq 1:

$$E_{CB} = X - E_c - 0.5E_g \quad (1)$$

where $E_c$ is the energy of free electrons on the hydrogen scale (4.5 eV), $X$ is the electronegativity of the semiconductor, and $E_g$ is the band-gap energy of the semiconductor.

The edge of the valence band ($E_{VB}$) of $Bi_2WO_6$ was determined to be 2.44 V (vs normal hydrogen electrode, NHE), more positive than that of $E^\circ(H_2O/H^+)$ ($H_2O \rightarrow {}^1/_2O_2 + 2H^+ + 2e^-$, $E^\circ_{redox}$ = 0.82 V vs NHE), and the edge of the conduction band was estimated to be −0.31 V (vs NHE), more negative than that of $E^\circ(CO_2/CH_4)$ ($CO_2 + 8e^- + 8H^+ \rightarrow CH_4 + 2H_2O$, $E^\circ_{redox}$ = −0.24 V vs NHE). This indicates that the photogenerated electrons and holes on the irradiated $Bi_2WO_6$ can react with adsorbed $CO_2$ and $H_2O$ to produce $CH_4$, as described in the following equation:

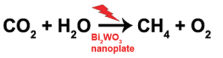


We perform $CO_2$ and gaseous $H_2O$ photocatalysis in a gas−solid system over the $Bi_2WO_6$ nanoplates in the absence of any cocatalysts under visible-light ($\lambda$ > 420 nm) irradiation. Gas chromatographic analysis shows that $CH_4$ was exclusively obtained as the reduction product without detectable $CH_3OH$, $H_2$, and CO as secondary products. The gross yield in $CH_4$ increased with the photolysis time (Figure 9a), and the total yield of $CH_4$ obtained in the experiment after 5.5 h of continuous irradiation was 6 $\mu$mol, corresponding to approximately 1.1 $\mu$mol/g·h of the $CH_4$ formation rate. A conversion experiment of $CO_2$ performed in the dark or in the absence of the photocatalyst shows no appearance of $CH_4$, proving that the reduction reaction of $CO_2$ is driven by light under the photocatalyst. In comparison, the SSR of $Bi_2WO_6$ shows trifling photocatalytic activity toward methane production (0.045 $\mu$mol/g·h; Figure 9b). The higher photocatalytic activity of the $Bi_2WO_6$ nanoplate toward the reduction of $CO_2$ than that of the SSR sample can be contributed to following three reasons: (1) Reducing the lateral dimension to the nanometer length scale with regard to the nanoplate offers a high specific surface area of 5.63 $m^2/g$, over 9 times larger than 0.6 $m^2/g$ of SSR materials. (2) The ultrathin geometry of the nanoplate allows charge carriers fast mobility from the interior onto the surface to participate in the photoreduction reaction. This should also favor the improved separation of photogenerated electron and hole and a lower electron−hole recombination rate. (3) Exposure of the {001} crystal plane of the nanoplates is much attributed to the enhanced photoreduction activity (see below).

Shape control shows a great versatility for tuning the photocatalytic properties of semiconductor materials. The photocatalytic

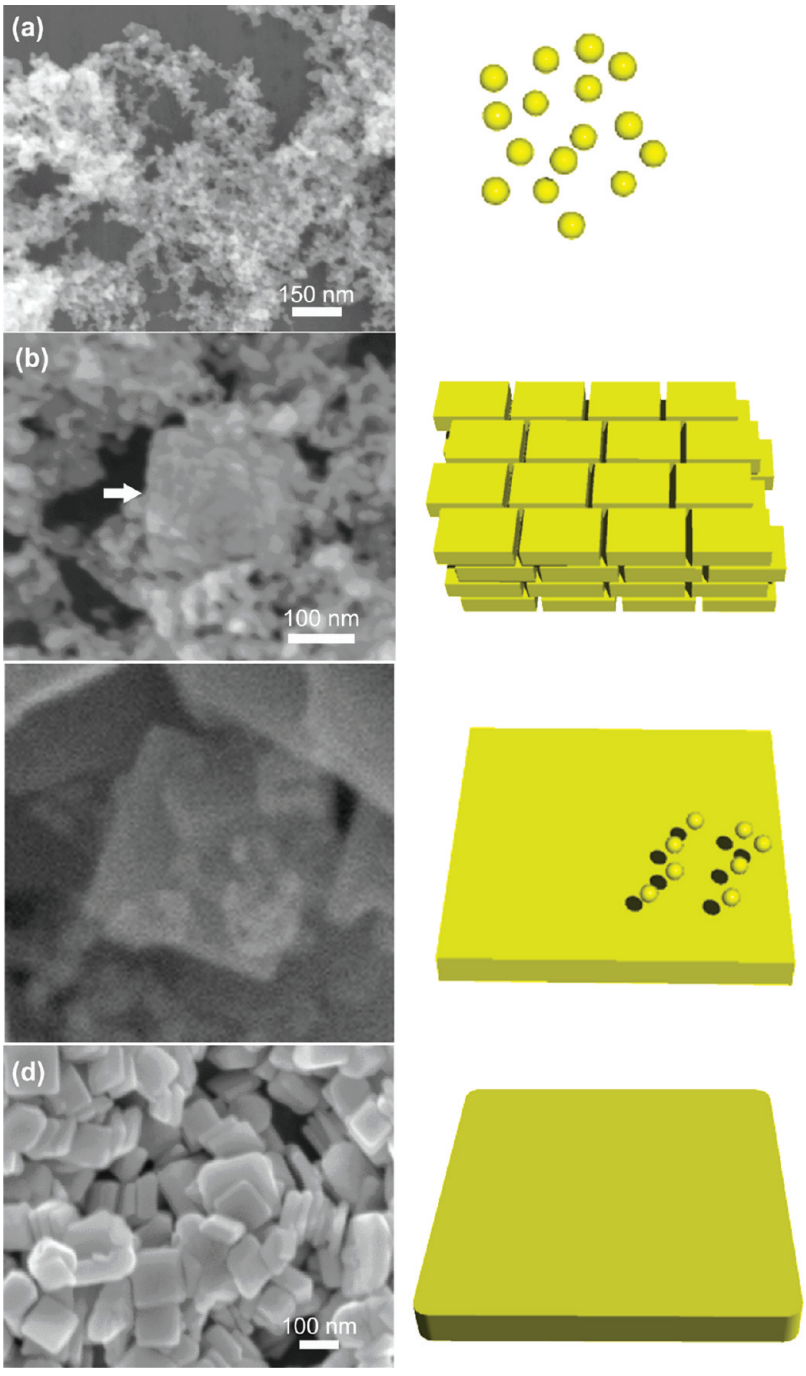


**Figure 5.** FESEM images (left panel) and corresponding schematic illustration (right panel) showing the evolution process of the nanoplate formation, a → b → c →d.

$CO_2$ conversion efficiency of nanocrystals into hydrocarbon can be significantly improved by tailoring the shape and the surface structure of the nanocrystals.[16] Many studies have demonstrated that CO was detected as the initial redox product of $CO_2$ photoreduction for the conversion of $CO_2$ into methane.[17] Thus, the activation and disassociation of $CO_2$ are considered vital steps for the photoreduction process (eq 2).

$$CO_2 + 2e^- + 2h^+ \rightarrow CO + O \quad (2)$$

Our calculation suggests that exposure of the {001} crystalline plane of the well-defined $Bi_2WO_6$ nanoplate is a prerequisite for a high level of photocatalytic activity; i.e., the {001} plane is more effective at the present photocatalysis reactions than other crystal planes. We carried out preliminary DFT calculations with the ultrasoft pseudopotential plane-wave method implemented in the CASTEP code.[18] We first optimized the adsorbed configurations for each slab model (gas $CO_2$, gas CO + O, adsorbed $CO_2$, and adsorbed CO + O), respectively, and then attempted to find the TSs

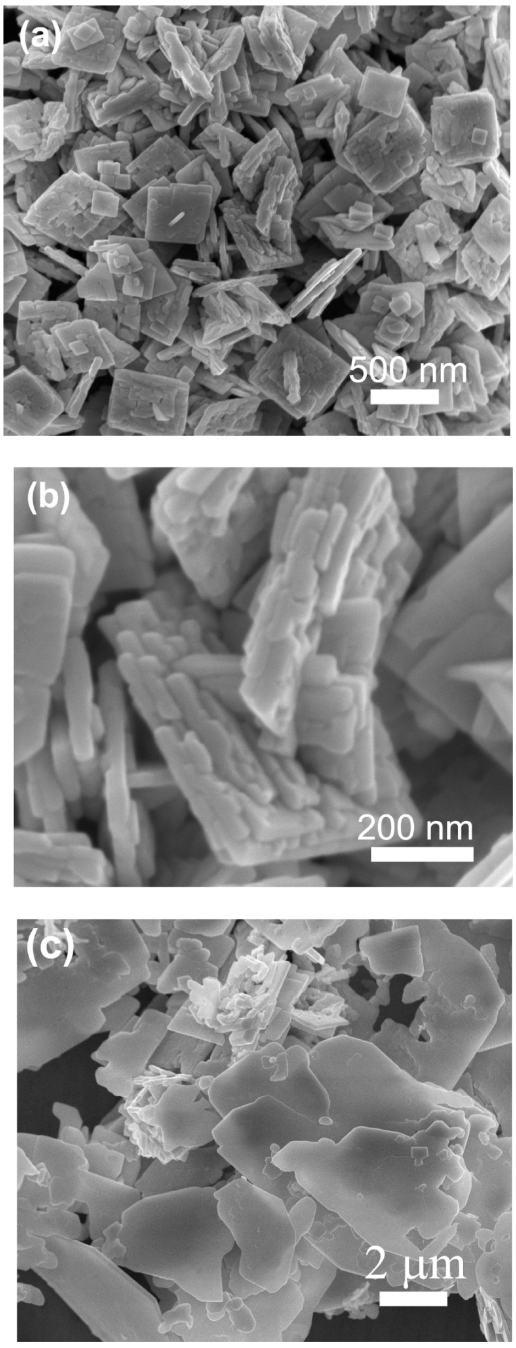


**Figure 6.** Different-magnification SEM images of (a and b) in-plane and out-of-plane amalgamation of the nanoplates formed at pH = ~5.5. (c) Large flakes produced at pH = ~10.5.

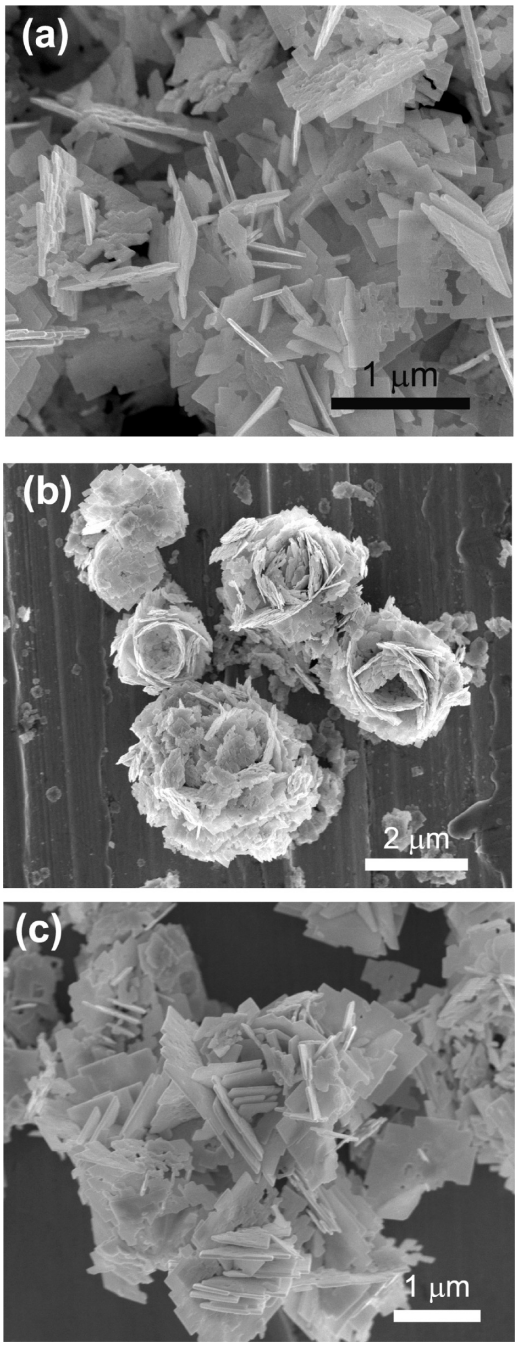


**Figure 7.** FESEM image of $Bi_2WO_6$ produced (a) in the absence of surfactants, (b) with CTAB, and (c) with L-lysine.

using complete LST/QST algorithms.[19] We select {001}, {010}, and {101} in this study to compare the photocatalytic dissociation reactivity of $CO_2$ among different crystalline planes. Our preliminary calculation in Figure 10 demonstrates that the adsorption energy of CO + O (0.487 eV) is larger than that of $CO_2$ (0.176 eV) on the {001} surface in contrast with {010} and {101} facets. This implies that $CO_2$ dissociation is thermodynamically preferred on the $Bi_2WO_6$ {001} surface. Meanwhile, the dissociation barrier of TS2 (4.773 eV, from the reactant) is smaller than that of TS1 (11.876 eV) and TS4 (13.444 eV), indicating that $CO_2$ dissociation on the $Bi_2WO_6$ {001} surface is easier than that in the gas phase and {101} surface. Although the dissociation barrier of TS3 (3.915 eV, from the reactant) is smaller than that of TS2, the energy barrier of the former from the product (1.214 eV, from the product) is much smaller than that of the latter, which means the dissociated CO + O on the {010} surface is easily recombined to $CO_2$ again. All of the analyses reveal that the $Bi_2WO_6$ {001} surface is a particular reactive surface energtically favoring the photoreduction of $CO_2$.

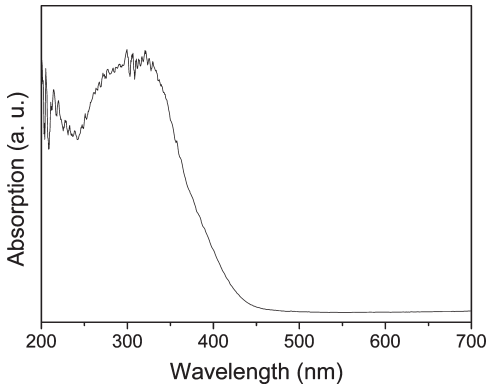


**Figure 8.** UV−vis diffuse-reflectance spectrum of the synthesized $Bi_2WO_6$ nanosquare.

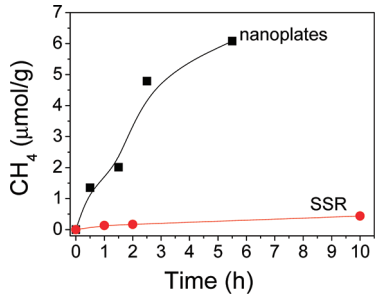


**Figure 9.** $CH_4$ generation over (a) nanoplates and (b) the SSR sample as a function of visible-light irradiation times ($\lambda$ > 420 nm).

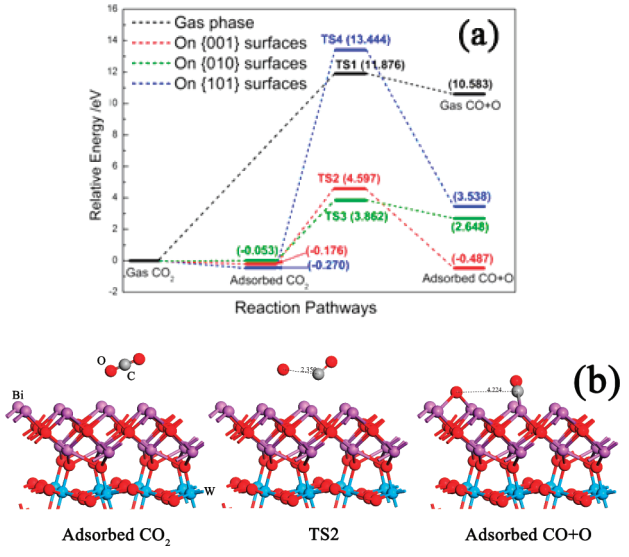


**Figure 10.** (a) Relative energy profile of the $CO_2$ dissociation pathways on different crystalline planes of $Bi_2WO_6$. The corresponding relative energy of each state is noted in the parent. (b) Optimized atomic structure models of $CO_2$ and its decomposed products adsorbed on the $Bi_2WO_3$ (001) surface. The red balls represent oxygen atoms, the gray balls represent carbon atoms, the purple balls represent bismuth atoms, and the blue balls represent tungsten atoms.

## CONCLUSION

Ultrathin and uniform $Bi_2WO_6$ platelike nanocrystallites have been successfully prepared and were found to induce $CO_2$ fixation under visible-light illumination. The $Bi_2WO_6$ sheets with the preferentially exposed {001} surface exhibited greatly enhanced photocatalytic activity. The ultrathin geometry of the nanoplates also promotes charge carriers to move rapidly from the interior to the surface to participate in the photoreduction reaction and should also favor an improved separation of the photogenerated electron and hole and the lower electron−hole recombination rate. While the photocatalytic reduction of $CO_2$ is still in its infancy, our results demonstrate a significant step toward making more efficient photocatalysts for $CO_2$ capture and reuse.

## AUTHOR INFORMATION

### Corresponding Author

*Tel: +86 25 8362 1372. E-mail: zhouyong1999@nju.edu.cn (Y.Z.), zgzou@nju.edu.cn (Z.Z.).

## ACKNOWLEDGMENT

This work was supported by 973 Programs (2011CB933300/2011CB933303 and 2007CB613305), JST-MOST (2009DFA61090), JSPS-NSFC (20811140087), NSFC (20971048 and 50732004), and Fundamental Research Funds for the Central Universities (1113020401).

## REFERENCES

(1) Kudo, A.; Hijii, S. *Chem. Lett.* **1999**, 1103.
(2) Tang, J. W.; Zou, Z. G.; Ye, J. H. *Catal. Lett.* **2004**, *92*, 53.
(3) (a) Amano, F.; Yamakata, A.; Nogami, K.; Osawa, M.; Ohtani, B. *J. Am. Chem. Soc.* **2008**, *130*, 17650. (b) Amano, F.; Nogami, K.; Abe, R.; Ohtani, B. *J. Phys. Chem. C* **2008**, *112*, 9320. (c) Wu, L.; Bi, J.; Li, Z.; Wang, X.; Fu, X. *Catal. Today* **2008**, *131*, 15. (d) Zhang, L.; Wang, W. Z.; Zhou, L.; Xu, H. *Small* **2007**, *3*, 1618. (e) Wu, J.; Duan, F.; Zheng, Y.; Xie, Y. *J. Phys. Chem. C* **2007**, *111*, 12866. (f) Zhang, C.; Zhu, Y. F. *Chem. Mater.* **2005**, *17*, 3537. (g) Yu, S. H.; Liu, B.; Mo, M. S.; Huang, J. H.; Liu, X. M.; Qian, Y. T. *Adv. Funct. Mater.* **2003**, *13*, 639. (h) Maczka, M.; Macalik, L.; Hermanowicz, K.; Kepinski, L.; Tomaszewski, P. *J. Raman Spectrosc.* **2010**, *41*, 1059. (i) He, D. Q.; Wang, L. L.; Li, H. Y.; Yan, T. Y.; Wang, D. J.; Xie, T. F. *Cryst. Eng. Commun.* **2011**, *13*, 4053.
(4) Gust, D.; Moore, T. A.; Moore, A. L. *Acc. Chem. Res.* **2009**, *42*, 1890.
(5) (a) Inoue, T.; Fujishima, A.; Konishi, S.; Honda, K. *Nature* **1979**, *277*, 637. (b) Halmann, M. *Nature* **1978**, *275*, 115.
(6) Barton, E. E.; Rampulla, D. M.; Bocarsly, A. B. *J. Am. Chem. Soc.* **2008**, *130*, 6342.
(7) See reviews: (a) Roy, S. C.; Varghese, O. K.; Paulose, M.; Grimes, C. A. *ACS Nano* **2010**, *4*, 1259. (b) Olah, G. A.; Goeppert, A.; Surya Prakash, G. K. *J. Org. Chem.* **2009**, *74*, 487. (c) Ikeue, K.; Yamashita, H.; Anpo, M.; Takewaki, T. *J. Phys. Chem. B* **2001**, *105*, 8350. (d) Kitano, M.; Matsuoka, M.; Ueshima, M.; Anpo, M. *Appl. Catal., A* **2007**, *325*, 1. (e) Indrakanti, V. P.; Kubicki, J. D.; Schobert, H. H. *Energy Environ. Sci.* **2009**, *2*, 745. (f) Dey, G. R. *J. Nat. Gas Chem.* **2007**, *16*, 217. (g) Usubharatana, P.; McMartin, D.; Veawab, A.; Tontiwachwuthikul, P. *Ind. Eng. Chem. Res.* **2006**, *45*, 2558.
(8) Liu, Q.; Zhou, Y.; Kou, J. H.; Chen, X. Y.; Tian, Z. P.; Gao, J.; Yan, S. C.; Zou, Z. G. *J. Am. Chem. Soc.* **2010**, *132*, 14385.
(9) (a) Varghese, O. K.; Paulose, M.; LaTempa, T. J.; Grimes, C. A. *Nano Lett.* **2009**, *9*, 731. (b) Yang, C. C.; Yu, Y. H.; van der Linden, B.; Wu, J. C. S.; Mul, G. *J. Am. Chem. Soc.* **2010**, *132*, 8398.
(10) (a) Nguyen, T. V.; Wu, J. C. S.; Chou, C. H. *Catal. Commun.* **2008**, *9*, 2073. (b) Ozcan, O.; Yukruk, F.; Akkaya, E. U.; Uner, D. *Top. Catal.* **2007**, *44*, 523.
(11) Woolerton, T. W.; Sheard, S.; Reisner, E.; Pierce, E.; Ragsdale, S. W.; Armstrong, F. A. *J. Am. Chem. Soc.* **2010**, *132*, 2132.

(12) Zou, Z. G.; Ye, J. H.; Sayama, K.; Arakawa, H. *Nature* **2001**, *414*, 625.
(13) (a) Gao, F.; Chen, X. Y.; Yin, K. B.; Dong, S.; Ren, Z. F.; Yuan, F.; Yu, T.; Zou, Z. G.; Liu, J. M. *Adv. Mater.* **2007**, *19*, 2889. (b) Lv, J.; Kako, T.; Li, Z. S.; Zou, Z. G.; Ye, J. H. *J. Phys. Chem. C* **2010**, *114*, 6157. (c) Kou, J. H.; Gao, J.; Li, Z. S.; Zou, Z. G. *Curr. Org. Chem.* **2010**, *14*, 728. (d) Fan, X. X.; Gao, J.; Wang, Y.; Li, Z. S.; Zou, Z. G. *J. Mater. Chem.* **2010**, *20*, 2865. (e) Lv, J.; Kako, T.; Zou, Z. G.; Ye, J. H. *J. Mater. Res.* **2010**, *25*, 159. (f) Lv, J.; Kako, T.; Zou, Z. G.; Ye, J. H. *Appl. Phys. Lett.* **2009**, *95*, 032107.
(14) Jing, L.; Sun, X.; Xin, B.; Wang, B.; Cai, W.; Fu, H. *J. Solid State Chem.* **2004**, *177*, 3375.
(15) Kudo, A.; Tsuji, I.; Kato, H. *Chem. Commun.* **2002**, 1958.
(16) (a) Anpo, M.; Yamashita, H.; Ichihashi, Y.; Ehara, S. *J. Electroanal. Chem.* **1995**, *396*, 21. (b) Yamashita, H.; Kamada, N.; He, H.; Tanaka, K.; Ehara, S.; Anpo, M. *Chem. Lett.* **1994**, *5*, 855.
(17) Li, S. F.; Guo, Z. X. *J. Phys. Chem. C* **2010**, *114*, 11456.
(18) Clark, S. J.; Segall, M. D.; Pickard, C. J.; Hasnip, P. J.; Probert, M. J.; Refson, K.; Payne, M. C. *Z. Kristallogr.* **2005**, *220*, 567.
(19) Govind, N.; Petersen, M.; Fitzgerald, G.; King-Smith, D.; Andzelm, J. *Comput. Mater. Sci.* **2003**, *28*, 250.